Exact relativistic kinetic theory of the full unstable spectrum of an electron-beam–plasma system with Maxwell-Jüttner distribution functions

A. Bret*
ETSI Industriales, Universidad de Castilla–La Mancha, 13071 Ciudad Real, Spain and Instituto de Investigaciones Energéticas y Aplicaciones Industriales, Campus Universitario de Ciudad Real, 13071 Ciudad Real, Spain

L. Gremillet† and D. Bénisti
CEA, DAM, DIF, F-91297 Arpajon, France
(Received 7 January 2010; published 8 March 2010)

Following a recent Letter by Bret *et al.* [Phys. Rev. Lett. **100**, 205008 (2008)], we present a detailed report of the entire unstable **k** spectrum of a relativistic collisionless beam-plasma system within a fully kinetic framework. In contrast to a number of previously published studies, our linear analysis makes use of smooth momentum distribution functions of the Maxwell-Jüttner form. The three competing classes of instabilities, namely, two-stream, filamentation, and oblique modes, are dealt with in a unified manner, no approximation being made regarding the beam-plasma densities, temperatures, and drift energies. We investigate the hierarchy between the competing modes, paying particular attention to the relatively poorly known quasielectrostatic oblique modes in the regime where they govern the system. The properties of the fastest growing oblique modes are examined in terms of the system parameters and compared to those of the dominant two-stream and filamentation modes.

DOI: 10.1103/PhysRevE.81.036402 PACS number(s): 52.35.Qz, 52.35.Hr, 52.50.Gj, 52.57.Kk

I. INTRODUCTION

The theory of electron-beam–plasma instabilities stands among the oldest and most thoroughly investigated topics in plasma physics [1] owing to its relevance in many fields ranging from fusion science [2–9] to astrophysics [10–18]. Six decades ago, Bohm and Gross noted that an electron beam passing through a collisionless plasma is unstable with respect to electrostatic perturbations propagating along the beam direction [19]. Later on, the seminal works of Weibel [20] and Fried [21] demonstrated that electromagnetic modulations normal to the flow or the high-temperature axis (Weibel) may also turn unstable. Both instability classes (hereafter referred to as two-stream and filamentation instabilities, respectively) were subsequently given more general descriptions accounting for arbitrarily oriented perturbations [3,22–27] and/or finite-size beam effects [28–32].

It is now understood that instabilities characterized by wave-vectors oblique or normal to the beam direction usually prevail in the relativistic regime [7,14,23,33–36]. Among these, the filamentation instability has as yet received most of the attention [37–47]. In contrast, oblique-propagating modes have been much less investigated due to the need of a two-dimensional (2D) relativistic formalism. Whereas a general electromagnetic formulation is required to describe the transition from oblique to filamentation modes, most of the initial investigations of oblique instabilities were based on the electrostatic approximation [23,24,26,48]. To our knowledge, the general kinetic dispersion relation was first numerically tackled by Lee and Thode [27] in the early 1980s for a special class of angularly spread mononergetic electron beams. They showed that the electrostatic limit underestimates the growth rates at large wave angles where unstable modes turn mostly electromagnetic. Their analysis, however, was restricted to weak beam densities and transverse temperatures and, in addition, fell short of addressing the oblique-to-filamentation transition. One had to wait more than a decade for the first picture of the entire 2D spectrum, albeit in the cold-fluid limit [49]. A first step toward the generalization of these results to the kinetic regime has recently been made by means of waterbag distribution functions [35,50–52]. Much simpler fluid formulations, either relativistically covariant [53] or not [54], have also been employed lately to assess thermal corrections. Even though waterbag-based kinetic approaches are helpful for a qualitative evaluation of thermal effects and in singling out the dominant unstable mode for a given set of parameters, they are severely flawed by their neglect of Landau damping and obvious inadequacy in modeling relativistic temperatures. The latter shortcoming is very limiting when handling high-energy beam-plasma systems, such as those generated, for instance, in relativistic laser-plasma interaction [45,55–57].

In a recent Letter [58], we reported on the first unified kinetic theory of the unstable spectrum of a relativistic beam-plasma system. Our main goal was then to determine the domain of preponderance of each instability class in the multidimensional parameter space, while briefly discussing a few properties about the transitions between two distinct instability classes. Here, we intend to further detail the technical aspects of the theory and to elaborate on its most salient features. The article is organized as follows. In Sec. II, we justify the choice of the Maxwell-Jüttner distribution function for the equilibrium configuration and present the numerical method used for solving the relation dispersion. Section III is devoted to a comprehensive examination of the hierarchy of the competing modes, including its major con-

*antoineclaude.bret@uclm.es
†laurent.gremillet@cea.fr

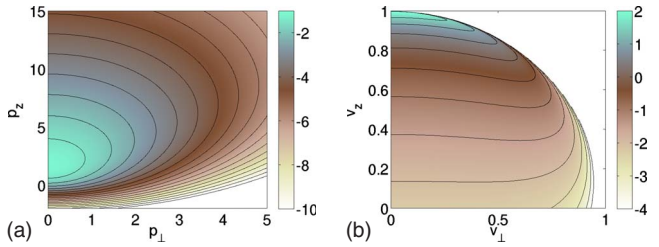

FIG. 1. (Color online) (a) Typical plot (in log scale) of Eq. (1) in the $(p_\perp, p_z)$ plane, where $p_\perp = \sqrt{p_x^2 + p_y^2}$. Parameters are $\gamma_j = 2$ and $T_j = 100$ keV. (b) Same distribution function plotted in the $(v_\perp, v_z)$ velocity plane.

sequences. Section IV explores the oblique-mode-dominated regime by studying the variations in the maximum growth rate and the associated wave vector with the beam parameters. We also confirm the mainly electrostatic character of the fastest growing oblique modes. Their investigation can therefore be considerably eased by means of the dispersion relation obtained under the electrostatic approximation, as carried out in the past for somewhat simpler configurations [23,24,26,48]. Finally, Sec. V gathers our concluding remarks and prospects.

II. FORMALISM

A. Equilibrium configuration

In order to deal with potentially relativistic thermal spreads, we model the unperturbed electron-beam–plasma system as a combination of drifting Maxwell-Jüttner distribution functions [59,60] of the form

$$f_j^0(\mathbf{p}) = \frac{\mu_j}{4\pi\gamma_j^2 K_2(\mu_j/\gamma_j)} \exp[-\mu_j(\gamma(\mathbf{p}) - \beta_j p_z)], \qquad (1)$$

where the index $j=(b,p)$ stands for the beam or plasma component, $\beta_j = \langle p_z/\gamma \rangle_j$ is the normalized z-aligned mean drift velocity, γ_j is the corresponding relativistic factor, and $\mu_j = m_e c^2/k_B T_j$ is the normalized inverse temperature of each electron component. All momenta are normalized to $m_e c$ and K_2 denotes a modified Bessel function of the second kind. The distribution function is normalized to unity: $\int f_j^0 d^3p = 1$. Charge and current neutralization is assumed so as to ensure a field-free equilibrium. This implies $n_b + n_p = Z n_i$ and $n_b \beta_b + n_p \beta_p = 0$, where n_i and Z are the ion density and charge, respectively. From now on, the ions form a fixed neutralizing background and collisions are neglected.

A typical plot of Eq. (1) is displayed in Fig. 1(a) with $\gamma_j = 2$ (i.e., $\beta_j = 0.87$) and $T_j = 100$ keV. In contrast to the nonrelativistic case, the distribution exhibits an asymmetric shape about the longitudinal momentum $\gamma_j \beta_j$ associated with the mean velocity. A high-energy tail arises from the Lorentz transform between the drifting frame and the laboratory frame. The same distribution is plotted in Fig. 1(b) as a function of the velocity variables, use being made of the Jacobian transformation $d^3p = \gamma^5 d^3v$. The function peaks near $v_z \sim 1$, with a transverse velocity spread

$$\Delta v_\perp \sim (2/\gamma_j \mu_j)^{1/2}, \qquad (2)$$

largely exceeding the longitudinal one

$$\Delta v_z \sim (\gamma_j^3 \mu_j)^{-1/2}. \qquad (3)$$

Note that the above estimates formally apply in the limit $\mu_j/\gamma_j \gg 1$, only marginally satisfied in the present case. As seen below, this anisotropy bears important consequences on the sensitivity of oblique modes to thermal spreads [23,24,26].

The Maxwell-Jüttner distribution constitutes the correct relativistic generalization of the standard Maxwellian distribution [59]. Its drifting expression (1) can be derived by maximizing the specific entropy for fixed values of each species' total momentum and energy [60]. The doubts that had emerged since the 1980s about the validity of the Jüttner distribution were recently ruled out by molecular dynamics simulations [61,62].

Two additional arguments can be made for using a Maxwell-Jüttner function. The first is that it allows for an exact treatment of the 2D axisymmetric case at an affordable numerical cost. The second is its ability, maybe fortuitous, to capture the main features of the momentum distribution of a laser-accelerated, relativistic electron filament [45]. One should note, though, that this function is not suited to modeling temperature anisotropy effects since it depends on only one thermal spread parameter. These effects may be accessed using waterbag functions [51,63] or the smooth, relativistic bi-Maxwellian functions introduced in Refs. [63–66].

B. Dielectric tensor and dispersion relation

The derivation of the dielectric tensor of an unmagnetized, homogeneous, and infinite relativistic beam-plasma system is a classic calculation [50,67]. The perturbations are taken in the form $\exp(i\mathbf{k}\cdot\mathbf{r} - i\omega t)$. Without loss of generality, it is sufficient to consider $\mathbf{k} = (k_x, 0, k_z)$ due to the axisymmetry of the system. The full three-dimensional (3D) problem is here dealt with from basic principles, so that the same dispersion relation is used to describe the two-stream instability for $k_x = 0$, the filamentation instability for $k_z = 0$ and the unstable oblique modes for intermediate orientations of the wave vector. This means, in particular, that no *a priori* approximation whatsoever is made regarding the polarization of the unstable modes. Regarding the number of dimensions considered, it is important to notice that although we can restrict the wave-vector phase space to 2D, the *velocity* space considered is 3D. In the nonrelativistic regime, and for separable distribution functions [i.e., $f(\mathbf{v}) = f_x(v_x) f_y(v_y) f_z(v_z)$], the quadratures involved in the dispersion relation can generally be reduced exactly from 3D to 2D by factorizing the integral along the y axis. In the present case, the distributions functions are not separable. Furthermore, the Lorentz factor couples the quadratures along the three velocity axis, preventing an easy calculation of the y integrals.

The linearization of the relativistic Vlasov-Maxwell set of equations yields the dispersion equation

$$(\omega^2 \epsilon_{xx} - k_z^2)(\omega^2 \epsilon_{zz} - k_x^2) - (\omega^2 \epsilon_{xz} + k_x k_z)^2 = 0, \qquad (4)$$

in terms of the dielectric tensor elements

$$\epsilon_{kl}(\omega,\mathbf{k}) = \delta_{kl} + \sum_{j=b,p} \frac{n_j}{\omega^2} \int\int\int \frac{p_k}{\gamma} \frac{\partial f_j^0}{\partial p_l} d^3p + \sum_{j=b,p} \frac{n_j}{\omega^2} \int\int\int \frac{p_k p_l}{\gamma^2} \frac{\mathbf{k}\cdot\partial f_j^0/\partial \mathbf{p}}{\omega - \mathbf{k}\cdot\mathbf{p}/\gamma} d^3p, \quad (5)$$

where $\gamma=\sqrt{1+p^2}$. The density of the jth electron component n_j is normalized to the total electron density. The oscillation frequency ω and the wave-vector $\mathbf{k}$ are respectively normalized to ω_e and ω_e/c, where ω_e is the nonrelativistic total plasma frequency. Inserting Eq. (1) into the tensor elements (5) yields a series of triple integrals which can be reduced to much more tractable one-dimensional quadratures following the lines of Ref. [60]. Changing to velocity variables in cylindrical coordinates along the wave vector $\mathbf{v}=(v_\perp \cos\varphi, v_\perp \sin\varphi, v_\parallel)$, the integrations in the $(v_\perp,\varphi)$ plane can be performed in closed form [60,68]. For each electron component j, the resulting simplified expressions of the tensor elements involve three one-dimensional quadratures $\mathcal{A}_j$, $\mathcal{B}_j$, and $\mathcal{C}_j$, which are reported in the Appendix.

C. Numerical solution of the dispersion equation

The dispersion relation (4) together with the tensor elements given by Eqs. (A1) and (A2) has been solved numerically for a complex ω as a function of a real $\mathbf{k}$. Introducing $\xi=\omega/k$, the integrals involved in the functions $\mathcal{A}$, $\mathcal{B}$, and $\mathcal{C}$ (the index j is henceforth omitted for the sake of simplicity) can be expressed in the general form

$$\mathcal{F} = \int_{-1}^{1} du \frac{g(u)}{u-\xi} \quad (\Im\xi > 0), \quad (6)$$

$$= \int_{-1}^{1} du \frac{g(u)-g(\xi)}{u-\xi} + g(\xi)\ln\left(\frac{\xi-1}{\xi+1}\right), \quad (7)$$

where the exact form of $g(u)$ depends on the function (i.e., $\mathcal{A}$, $\mathcal{B}$, or $\mathcal{C}$) under consideration, and ln denotes the principal branch of the complex logarithm. This formulation enables to remove the singularity of the integrand which can now be evaluated by means of any standard quadrature scheme.

The analytic continuation of the dispersion relation to the $\Im\xi<0$ half-plane directly follows from the above expression by adding the extra term $2i\pi g(\xi)$, that is, the value of the discontinuity jump of $\ln(\xi-1/\xi+1)$ across the real axis. We then have to choose the branch cuts of the multivalued functions involved in Eq. (A2). To be consistent with the branch cuts $]-\infty,-1[\cup]1,\infty[$ of the logarithm term, we choose the same branch cuts for the relativistic factor $\gamma=\sqrt{1-u^2}$. Accordingly, we make use of the expression

$$\gamma = i(r_+ r_-)^{-1/2}\exp[-i(\phi_+ + \phi_-)/2], \quad (8)$$

where $r_\pm=|u\pm 1|$ and the phase angles $\phi_\pm=\arg(u\pm 1)$ are restricted to the ranges $0<\phi_-<2\pi$ and $-\pi<\phi_+<\pi$.

Furthermore, the function $h(u)=\sqrt{\rho^2-\nu^2}$ is expressed as

$$h(u) = \mu|\beta|\gamma\sqrt{(u-\alpha_+)(u-\alpha_-)}, \quad (9)$$

where the roots $\alpha_\pm$ are given by

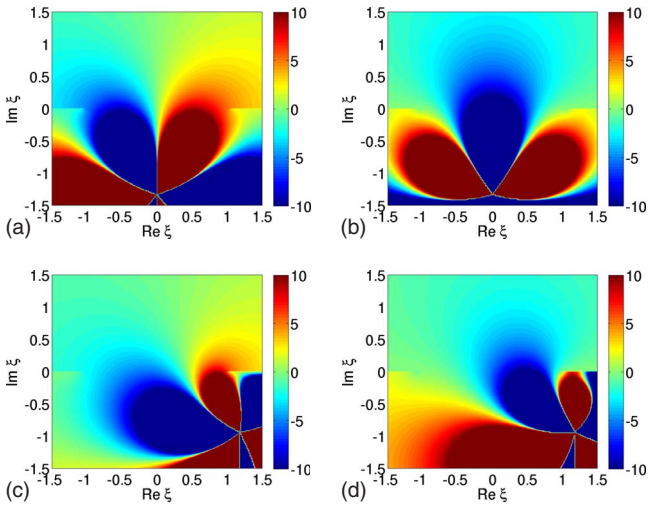

FIG. 2. (Color online) Maps in the complex ξ plane of the real (left) and imaginary (right) parts of the function $\mathcal{A}$ as given by Eq. (A2) for $\beta=0.6$, $\mu=1$, $\theta=\pi/2$ (a) and (b) and $\theta=\pi/4$ (c) and (d).

$$\alpha_\pm = \frac{\cos\theta}{\beta} \pm i \sin\theta\sqrt{1/\beta^2-1}, \quad (10)$$

and θ is the angle between $\mathbf{k}$ and the flow (z axis). The relativistic factor is computed as before, whereas we express

$$\sqrt{(u-\alpha_+)(u-\alpha_-)} = \sqrt{s_+ s_-}\exp[i(\zeta_+ + \zeta_-)/2]. \quad (11)$$

We have defined $s_\pm=|u-\alpha_\pm|$ and the phase angles $\zeta_\pm$ are now restricted to the ranges $-3\pi/2<\zeta_+<\pi/2$ and $-\pi/2<\zeta_-<3\pi/2$. These choices result in the branch cuts $]-\infty,-1[\cup]1,\infty[\cup]\alpha_- - i\infty,\alpha_-[\cup]\alpha_+,\alpha_+ + i\infty[$ for the function $h(u)$. As is evident from the analytical continuation following Eq. (7), the integrals $\mathcal{A}$, $\mathcal{B}$, and $\mathcal{C}$ inherit the branch cut $]\alpha_- - i\infty,\alpha_-[$ in the lower half ξ plane. By contrast, they are of the Cauchy type in the upper half ξ plane, and therefore everywhere holomorphic.

These properties are illustrated in Fig. 2 which plots the real and imaginary parts of the function $\mathcal{A}$ for $\beta=0.6$ and $\mu=1$. Two values of the wave-vector direction $\theta=\pi/2$ (a) and (b) and $\theta=\pi/4$ (c) and (d) are considered, yielding branch points at $\alpha_-=-1.33i$ and $\alpha_-=1.18-0.94i$, respectively. The branch cuts along $]-\infty,-1[,]1,\infty[$ and $]\alpha_- - i\infty,\alpha_-[$ clearly stand out, as does the analytic character of $\mathcal{A}$ in the upper half ξ plane. As can be easily demonstrated, and in contrast to the functions $\mathcal{B}$ and $\mathcal{C}$, $\mathcal{A}$ does not diverge at $\xi=\pm 1$.

The dispersion relation is solved using the nonlinear solver STRSCNE developed in Refs. [69,70]. The initial guess needed by the algorithm is provided either by the solution of the cold-fluid model [33] or by extrapolating the unstable solutions, if they exist, found at neighboring points on a (k_x,k_z) grid. However, this strategy may fail when handling high temperatures and/or a limited unstable domain, in which case we proceed iteratively by increasing progressively the temperature from zero to the final desired value, the solution obtained at each step serving as the initial estimate for the next one. Despite the analytical reduction of the

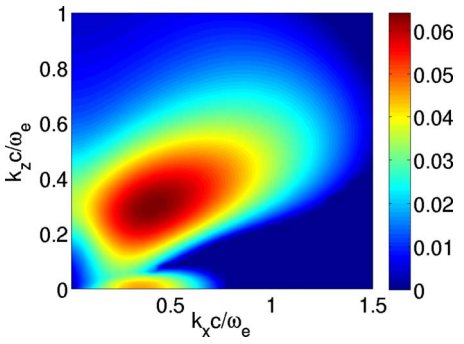

FIG. 3. (Color online) Normalized growth rate δ/ω_e as a function of the wave vector. Parameters are $n_b/n_p=1$, $\gamma_b=1.5$, $T_b=2000$ keV, and $T_p=5$ keV.

dispersion relation, this technique, if efficient enough, remains relatively time consuming for parametric investigations: a growth rate map on a 50×50 **k**-grid, such as those displayed in the following, takes on average several hours of calculation on a 3.4 GHz Intel Pentium 4 processor.

Typical variations in the growth rate $\delta=\Im\omega$ in the **k** space are displayed in Fig. 3 for $n_b/n_p=1$, $\gamma_b=1.5$, $T_b=2000$ keV, and $T_p=5$ keV. Two-stream modes are located along the z-aligned flow axis, and their growth rate peaks at $k_z c/\omega_e\sim0.3$. Filamentation modes have their wave vector oriented along the horizontal x axis, with a maximum growth rate at $k_x c/\omega_e\sim0.4$. Oblique modes have $k_x\neq0$ and $k_z\neq0$ and turn out to prevail for the chosen parameters. A major qualitative difference with previous results obtained in the relativistic regime with waterbag distributions [35,51] is the bounded character of the 2D unstable spectrum resulting from the Landau damping arising at large $|\mathbf{k}|$.

III. HIERARCHY OF UNSTABLE MODES

A. Frontiers between the various regimes

As illustrated in Fig. 3, beam-plasma systems are generally subject to a broad continuum of unstable modes belonging to distinct instability classes. The identification of the dominant mode is therefore required to predict the linear evolution of a system characterized by a given set of parameters. Because the three instability classes do not share the same sensitivity to the drift velocities, temperatures, and densities, they each govern different regions of the $(\gamma_b,T_b,T_p,n_b/n_p)$ parameter space. In the cold-fluid limit (i.e., $T_j=0$), it can thus be shown that, depending on γ_b, the filamentation instability tends to dominate for high beam densities $n_b/n_p\gtrsim0.53$ [71], while oblique modes eventually prevail for high enough γ_b, providing $n_b/n_p<1$ [72]. The determination of the mode hierarchy accounting for thermal effects is a rather painstaking task, which has been accomplished in Ref. [58] for a fixed (5 keV) plasma temperature.

For a given beam-plasma system, let us define δ_{TS}, δ_{F}, and δ_{O} the maximum growth rates of the two-stream, filamentation, and oblique modes, respectively. These three quantities correspond to the local growth rate maxima found along, or inside, the three identified parts of the **k** space (i.e., the parallel and transverse directions and the oblique region),

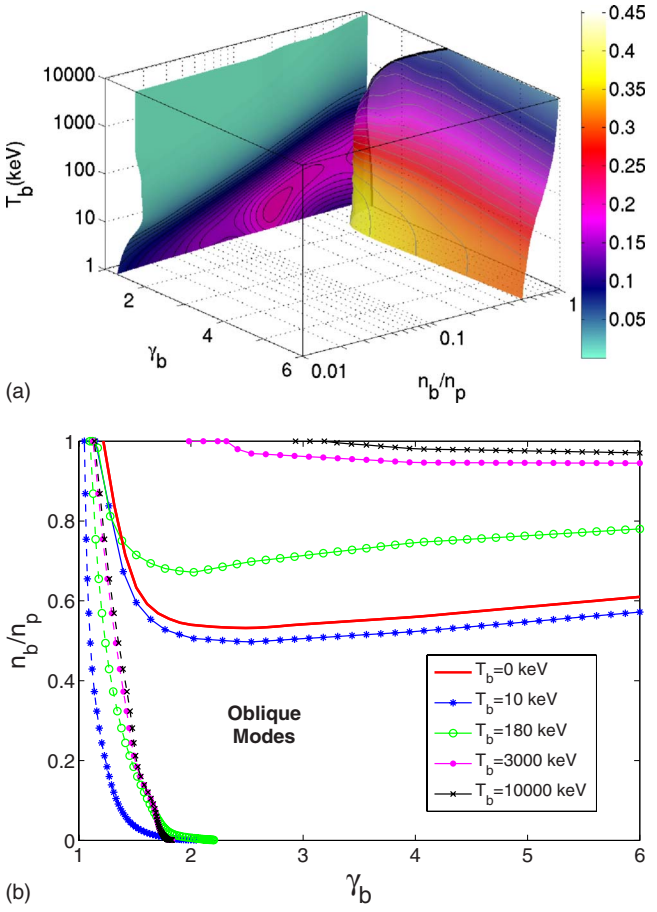

FIG. 4. (Color online) (a) Surface boundaries between the three instability regimes in the parameter space for $T_p=5$ keV. The left surface delimits the two-stream domain (at low γ_b) and the oblique-mode domain, whereas the right surface delimits the filamentation domain (at high n_b/n_p) and the oblique-mode-dominated domain. The color code visualizes the growth rate of the locally dominant mode, (b) two-stream/oblique boundaries (dashed) and filamentation/oblique boundaries (plain) for varying T_b. The bold line plots the oblique/filamentation boundary in the cold-fluid limit [71].

as illustrated in Fig. 3. For a fixed plasma temperature T_p, the equations $\delta_{\mathrm{TS}}=\delta_{\mathrm{O}}$ and $\delta_{\mathrm{TS}}=\delta_{\mathrm{F}}$ define two "surfaces boundaries" of the reduced parameter space $(\gamma_b,T_b,n_b/n_p)$. These surfaces therefore delimit domains of the parameter space in which the dominant mode of a given instability class grows faster than the dominant modes of the two other instability classes. Figure 4(a) displays the surface boundaries obtained for a 5 keV plasma. An alternate view of the mode hierarchy is shown in Fig. 4(b), which plots the boundaries corresponding to varying beam temperatures, together with the cold-fluid result [71]. Two-stream modes rule systems located on the low-γ_b side of the two-stream/oblique boundary, whereas filamentation modes rule systems located on the high n_b/n_p side of the filamentation/oblique boundary.

The shape of the two-stream/oblique frontier can be understood in terms of a balance between thermal and relativistic effects. It has long been understood that oblique modes are more sensitive to thermal effects than parallel modes [26,35,51]. This mostly stems from the fact that, as evi-

denced in Fig. 1(b) and Eqs. (2) and (3), the transverse velocity spread of a relativistic beam increases more rapidly with the temperature than the parallel spread. As a result, raising the beam temperature will preferentially affect oblique waves through kinetic effects, leading to an increasingly weakened growth rate. On the other hand, the γ_b dependence of the boundary results from the anisotropic relativistic inertia: when subject to a perturbing force, the longitudinal beam inertia ($\propto\gamma_b^3$) increases more rapidly with the relativistic factor than the transverse inertia ($\propto\gamma_b$), hence easing the amplification of transverse oscillations. Simply put, as highlighted in Figs. 4(a) and 4(b), the two-stream instability is more resistant to high temperatures than to high relativistic factors.

The filamentation/oblique transition is somewhat more involved than the two-stream/oblique transition, since it stems from a balance between the three system parameters. The filamentation growth rate increases with n_b/n_p, decreases with T_b but varies nonmonotonously with γ_b. This can be readily explained from the cold-fluid growth rate $\propto\beta_b/\sqrt{\gamma_b}$, which vanishes in both limits $\gamma_b\to 1$ and $\gamma_b\to\infty$, while reaching its maximum for $\gamma_b=\sqrt{3}$. As a result, provided the beam is not too hot, the extension of the filamentation-ruled domain is at its largest for moderately relativistic systems ($\gamma_b\sim 2$), whereas the filamentation modes are always surpassed for γ_b close to unity.

In the relativistic and ultrarelativistic regimes, the main parameter determining the filamentation/oblique transition is the beam density, even though it is always possible to reach the oblique regime for a hot enough beam. The latter result goes against the conventional belief that relativistic systems with $n_b/n_p=1$ are systematically governed by filamentation [73,74]. Yet the corresponding threshold temperature dramatically increases with γ_b. Figure 4(b) shows, for example, that a $n_b/n_p=1$ and $\gamma_b=3$ system is ruled by filamentation as far as $T_b<10$ MeV. Although the precise shape of the frontier evidently depends on the model distribution function, this result will hold, we think, at least qualitatively for a wide range of initial conditions. In particular, it provides a basis for a number of works dedicated to the filamentation instability in the context of the fast ignition approach to laser fusion [4,40,45,46,75,76]. This scheme relies on the ability of a PW laser-accelerated electron beam to heat a precompressed pellet up to ignition temperatures. In the vicinity of the laser absorption region, where the fast electron generation takes place, the beam and plasma densities should be comparable. The filamentation instability should therefore dominate the first stage of the beam transport, a prediction confirmed by a number of particle-in-cell simulations [55,56,77]. Given the major influence of this instability on the beam divergence, upon which the beam-target coupling efficiency critically depends [78], we will devote a separate paper to a thorough study of its properties [68].

Another interesting feature concerning the filamentation/oblique boundary is that the beam-to-plasma density ratio needed to switch to the filamentation regime approaches unity for increasingly large γ_b. From a numerical fit, we thus find that $1-n_b/n_p$ roughly behaves as $\gamma_b^{-1/3}$ in the large γ_b limit. Therefore, unless $n_b/n_p=1$, oblique modes govern the ultrarelativistic regime. This result is of great interest for astrophysical scenarios, where gamma factors up to 10^8 may be considered [13].

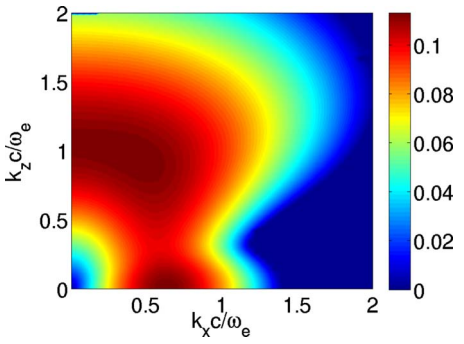

FIG. 5. (Color online) Growth rate map for $n_b/n_p=1$, $\gamma_b=1.1$, $T_b=100$ keV, and $T_p=5$ keV. The three instability classes are found to share almost the same maximum growth rate.

B. Transition from one regime to another

A system which representative point lies on one of the boundaries displayed in Figs. 4(a) and 4(b) is generally subject to a continuum of modes of different kinds growing at the same rate. A close examination of Fig. 4(a) even reveals that the surface boundaries almost make contact for $n_b/n_p=1$, $\gamma_b=1.1$, and $T_b=100$ keV. The corresponding unstable spectrum, depicted in Fig. 5, indeed confirms that the three instability classes share an approximately equal maximum growth rate $\delta=0.11$. Besides, a continuum of equally growing modes with $k_z\sim 1$ is seen to extend from $k_x=0$ to $k_x\sim 0.6$. For all its academic interest, this peculiar configuration arises for a unique "triple point" in the parameter space for a given plasma temperature. Far more representative are those systems located on a surface boundary, which correspond to a transition from one regime to another.

1. Filamentation-to-oblique transition

Let us first illustrate the filamentation-to-oblique transition. To this goal, we set $\gamma_b=3$, $T_b=500$ keV, and $T_p=5$ keV, and track the evolution of the spectrum when decreasing n_b/n_p from 1 to 0.1. Four such calculations are displayed in Fig. 6. As expected, the filamentation instability initially prevails until the transition point is reached for $n_b/n_p\sim 0.85$, below which oblique modes dominate. For $n_b/n_p=0.1$ [Fig. 6(d)], the filamentation modes are almost completely stabilized, their maximum growth rate being one order of magnitude lower than the maximum oblique-mode growth rate ($\delta_{\max}=0.012$). We now turn to Fig. 7 where k_x is kept fixed at 0.6, which corresponds to the fastest growing filamentation mode. This enables to highlight the *discontinuous* variation of the wave vector of the dominant mode during the transition. In this particular case, the dominant mode jumps from $k_z=0$ to ~ 0.45 around $n_b/n_p\sim 0.85$. Note that only the fastest growing wave vector is discontinuous: the growth rate $\delta(n_b/n_p, T_j, \gamma_b, \mathbf{k})$ is continuous, as is the absolute maximum growth rate. This result merely implies that the dominant oblique mode does not originate from the k_x axis, that is, from a displacement or a splitting of the domi-

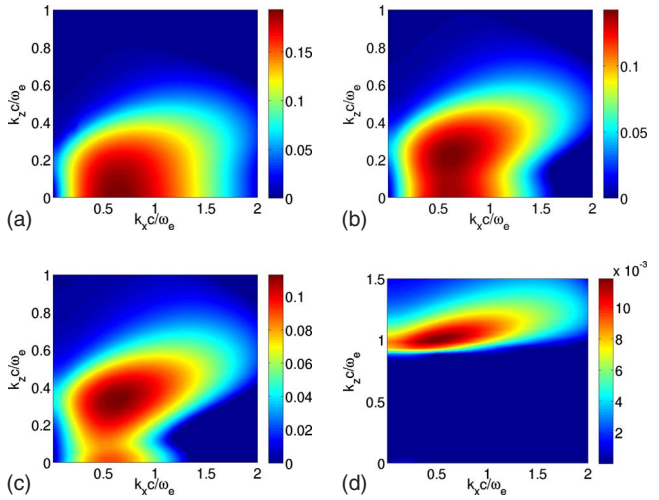

FIG. 6. (Color online) Growth rate maps for $\gamma_b=3$, $T_b=500$ keV, $T_p=5$ keV, and varying density ratios: (a) $n_b/n_p=0.9$, (b) $n_b/n_p=0.8$, (c) $n_b/n_p=0.7$, and (d) $n_b/n_p=0.1$.

nant filamentation mode. That the unstable spectrum exhibits two local maxima throughout the transition is further evidenced in the growth rate maps of Fig. 8. In contrast to the previous case, the filamentation-to-oblique transition is here triggered by raising the beam temperature from 100 to 500 keV. The other parameters are fixed at $\gamma_b=1.2$, $n_b/n_p=1$, and $T_p=5$ keV. For $T_b=300$ keV, the still dominant filamentation instability coexists with almost equally growing oblique modes [Fig. 8(b)]. The latter take over for $T_b=400$ keV [Fig. 8(c)], but the two instabilities remain connected by a strip of unstable modes, which gets increasingly thin with growing beam temperatures [Fig. 8(d)].

As far as could be checked numerically for other sets of parameters, the filamentation-to-oblique transition systematically gives rise to a discontinuous variation in k_z, in the absence of any measurable jump of k_x. This k_z discontinuity could play a major role in the nonlinear evolution of the beam-plasma system through its effect on the phase velocity of the dominant wave

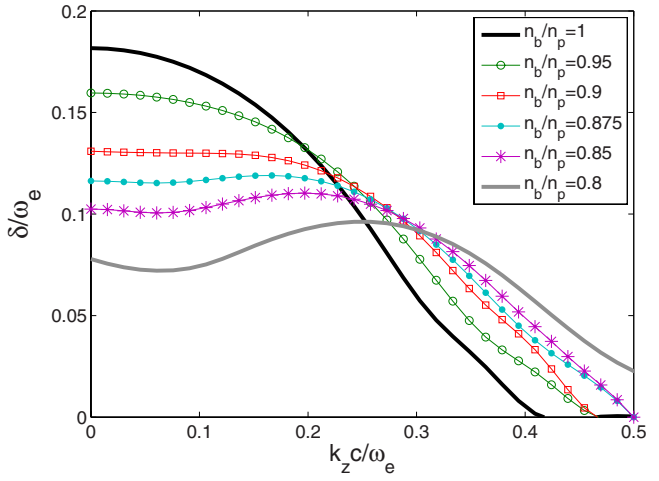

FIG. 7. (Color online) Growth rate vs k_z for $k_x=0.6$ and the same parameters as Fig. 6. The most unstable wave vector is found at $k_z=0$ for $n_b/n_p>0.85$, and $k_z\sim0.45$ when $n_b/n_p<0.85$.

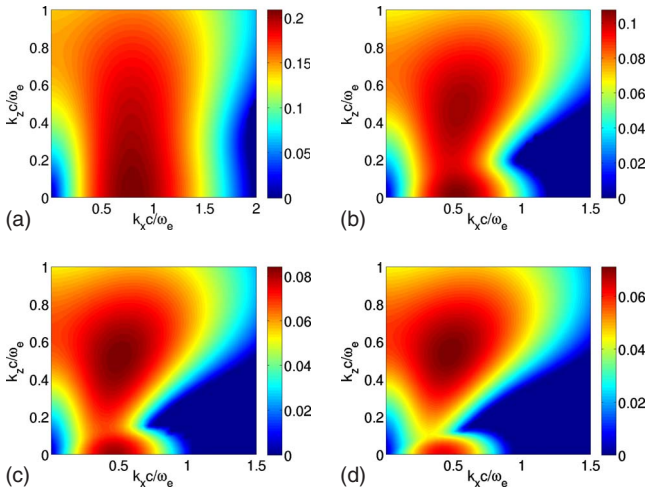

FIG. 8. (Color online) Growth rate maps for $\gamma_b=1.2$, $n_b/n_p=1$, $T_p=5$ keV, and varying beam temperatures: (a) $T_b=100$ keV, (b) $T_b=300$ keV, (c) $T_b=400$ keV, and (d) $T_b=500$ keV.

$$\mathbf{v}_\varphi = \Re\omega \frac{\mathbf{k}}{k^2}. \tag{12}$$

Filamentation modes, with $\Re\omega=0$, have zero phase velocity and are generally mostly electromagnetic [41,79], while oblique modes have a finite phase velocity and are quasielectrostatic [35,50,80]. As an example of the change in the characteristics of the dominant mode arising around the transition point, we display in Figs. 9(a) and 9(b) the maps of the real frequency and wave phase velocity corresponding to the parameters of Fig. 8(b), that is, for equal oblique and filamentation growth rates. In this equal-density case, the real frequency of the dominant oblique mode is comparable to its growth rate ($\Re\omega\sim0.075$), from which follows a nonzero, yet moderate, phase velocity $v_\varphi\sim0.1$. This contrasts with the zero wave phase velocity of the nonoscillating main filamentation mode.

2. Two-stream-to-oblique transition

As is clear from Figs. 4, the two-stream-to-oblique transition is mostly controlled by the beam relativistic factor. This transition is illustrated by the growth rate maps of Fig. 10 corresponding to $n_b/n_p=0.05$, $T_b=50$ keV, and $T_p=5$ keV. For $\gamma_b=1.5$, the dominant mode grows with $\delta_{\max}=0.37$ and is located at $(k_x,k_z)=(1.4,0)$ [Fig. 10(a)]. Raising the beam relativistic factor to $\gamma_b=2.5$ increases the maxi-

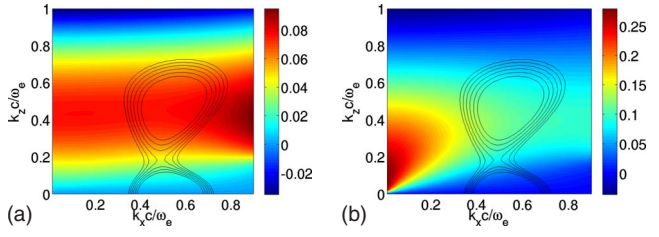

FIG. 9. (Color online) Normalized real frequency (a) and phase velocity modulus (b) for the parameters of Fig. 8(b). The contour lines plot the corresponding growth rate.

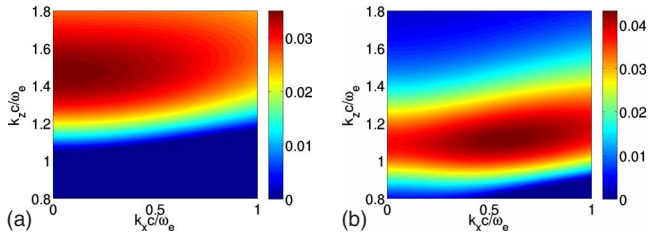

FIG. 10. (Color online) Growth rate maps for $n_b/n_p=0.05$, $T_b=50$ keV, $T_p=5$ keV, and varying beam relativistic factors: (a) $\gamma_b=1.5$ and (b) $\gamma_b=2.5$.

mum growth rate to $\delta_{\max}=0.43$, now located off axis at $(k_x,k_z)=(1.1,0.6)$ [Fig. 10(b)]. As hinted at by these two maps and in contrast to the filamentation-to-oblique transition, the system now switches continuously between two essentially similar regimes, which are characterized by quasielectrostatic modes (two-stream modes are even purely electrostatic) and finite wave phase velocities. This behavior is illustrated by the line outs of Fig. 11, where we have set $k_z=1$, $n_b/n_p=0.05$, $T_b=50$ keV, $T_p=5$ keV, and varied γ_b from 1.8 (two-stream regime) to 2.5 (oblique regime). One can see that the fastest growing mode smoothly connects with the k_z axis as the system enters the two-stream regime [58].

The maps of the real frequency and wave phase velocity for the parameters of Fig. 10(b) are shown in Figs. 12. The real frequency proves almost constant ($\Re\omega\sim 0.9$) along the line $k_z\sim 1.1$ linking the fastest growing two-stream and oblique modes. The wave phase velocity of the dominant oblique mode ($v_\varphi\sim 0.71$) is therefore reduced compared to that of the dominant two-stream mode ($v_\varphi\sim 0.82$). This reduction increases for larger transverse wave vectors, that is, as will be shown in Sec. IV B, for increasingly cold beams, in which case we have approximately

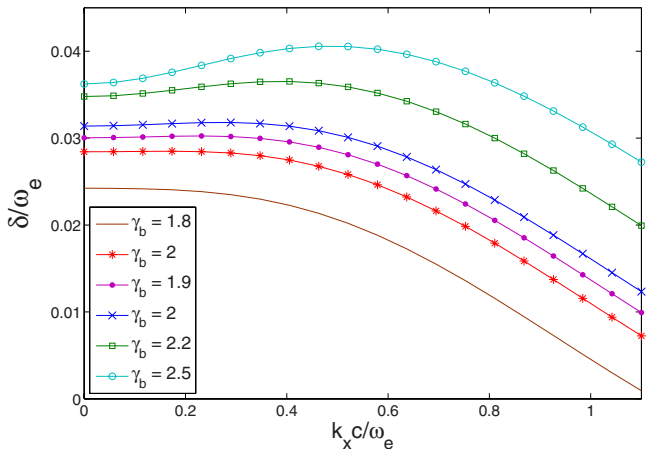

FIG. 11. (Color online) Growth rate δ vs k_x for $k_z=1$, $n_b/n_p=0.05$, $T_b=50$ keV, and $T_p=5$ keV. The beam relativistic factor increases from $\gamma_b=1.8$ (two-stream regime) to $\gamma_b=2.5$ (oblique regime). The most unstable wave vector evolves continuously between the two regimes.

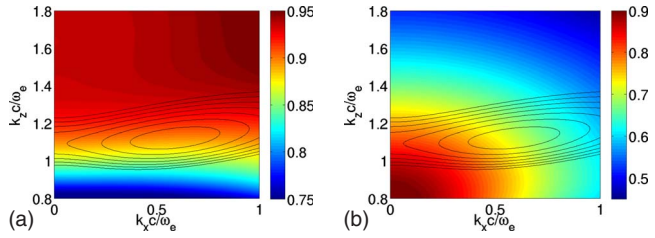

FIG. 12. (Color online) (a) Normalized real frequency and (b) phase velocity modulus for the parameters of Fig. 10(b). The contour lines plot the corresponding growth rate.

$$\mathbf{v}_\varphi \sim \frac{\beta_b}{\sqrt{1+k_x^2/k_z^2}}\frac{\mathbf{k}}{|\mathbf{k}|}. \tag{13}$$

Note that the slower phase velocities of oblique modes may accelerate the conversion of beam energy loss into plasma heating in the nonlinear regime [35,80].

IV. OBLIQUE-MODE DOMINATED REGIME

As previously mentioned, the filamentation-dominated regime in case of Maxwell-Jüttner distributions will be addressed in a separate, forthcoming publication [68]. Since a number of relativistic kinetic theories of the two-stream instability can be found in the literature [81–83], we find it worthwhile to concentrate on the somewhat lesser-known oblique regime for a detailed examination of the corresponding fastest growing mode. According to Figs. 4, oblique modes govern the evolution of rather diluted relativistic beams. The following analysis will therefore be restricted to this domain. Our objective here is to numerically explore the γ_b, n_b/n_p, and T_b variations in the dominant oblique mode so as to check, in particular, the validity of existing formulas [23,24,26,84].

A. Maximum growth rate

For $n_b/n_p\ll 1$ and $k_z\beta_b\sim 1$, the growth rate of the oblique modes reads in the cold-fluid (hydrodynamic) limit [3,24],

$$\delta^{\text{cold}} = \frac{\sqrt{3}}{2^{4/3}}\left(\frac{n_b}{\gamma_b n_p}\right)^{1/3}\left[\frac{k_x^2}{k^2}+\frac{1}{\gamma_b^2}\frac{k_z^2}{k^2}\right]^{1/3}. \tag{14}$$

This formula is derived assuming the oblique modes are of electrostatic character (i.e., satisfying $\mathbf{k}\times\mathbf{E}=0$), which is well verified in a broad parameter range. The maximum growth rate is thus obtained for $k_x\gg k_z$,

$$\delta_{\max}^{\text{cold}} = \frac{\sqrt{3}}{2^{4/3}}\left(\frac{n_b}{\gamma_b n_p}\right)^{1/3}. \tag{15}$$

The above expressions are valid as long as the beam velocity spread satisfies $|\mathbf{k}\cdot\Delta\mathbf{v}|<\delta$. Noting that the cold-fluid growth rate significantly decreases for $k_x\lesssim 1$ only, and using the low-temperature estimate Eq. (2), it follows that thermal effects set in when

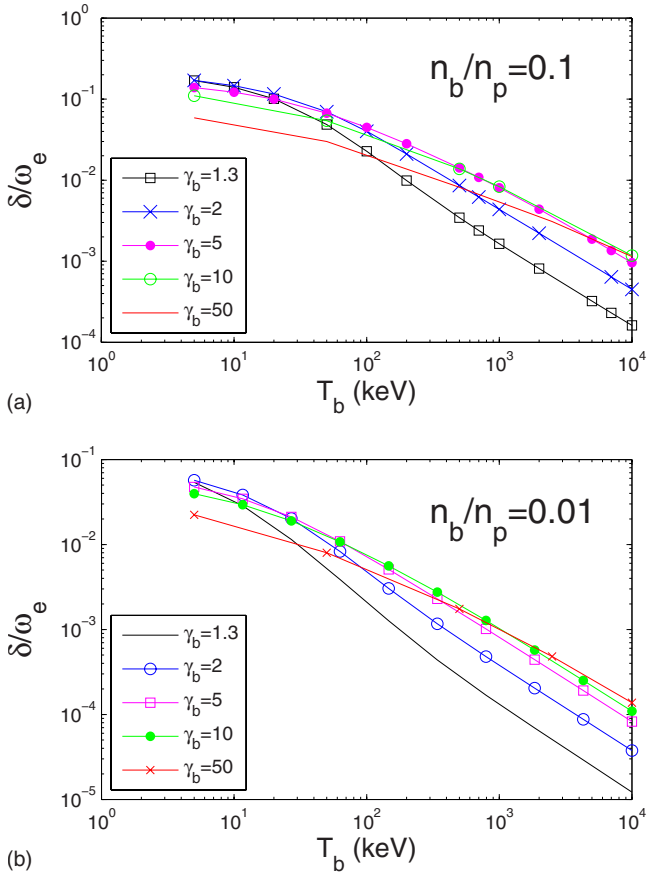

FIG. 13. (Color online) Maximum oblique growth rate $\delta_{\max}$ vs T_b for varying γ_b and (a) $n_b/n_p=0.1$ and (b) 0.01. $T_p=5$ keV in all cases. In the high-T_b limit, $\delta_{\max}$ scales like T_b^{-1} for any γ_b.

$$\frac{T_b}{m_e c^2} \gtrsim \frac{3}{2^{10/3}} \left(\frac{n_b}{n_p}\right)^{2/3} \gamma_b^{1/3} \frac{(1+\gamma_b^{-2})^{2/3}}{(1+\gamma_b^{-1})^2}, \tag{16}$$

where it has been assumed that $\gamma_b T_b/m_e c^2 \ll 1$. The system then enters the kinetic regime characterized by a weaker growth rate [3]

$$\delta_{\max}^{\mathrm{kin}} \sim \left(\frac{\beta_b}{\Delta v_\perp}\right)^2 \frac{n_b}{\gamma_b n_p}, \tag{17}$$

which, in the present case, may be approximated as

$$\delta_{\max}^{\mathrm{kin}} \sim \beta_b^2 \frac{m_e c^2}{T_b} \frac{n_b}{n_p}. \tag{18}$$

Note that the expression (17) applies in principle for a different unperturbed distribution than ours, namely, an angularly spread monoenergetic beam [3]. Even though, as shown below, it is found to overestimate by a factor ~5 the exact growth rates, it gives reliable T_b and n_b/n_p scaling laws, which, by the way, prove similar to those of the kinetic two-stream instability.

In order to assess the range of validity of the above formulas, we first plot the numerically obtained growth rate $\delta_{\max}$ vs T_b for varying γ_b and two values of the beam density $n_b/n_p=0.1$ [Fig. 13(a)] and 0.01 [Fig. 13(b)]. The plasma temperature is fixed at $T_p=5$ keV. In agreement with Eq.

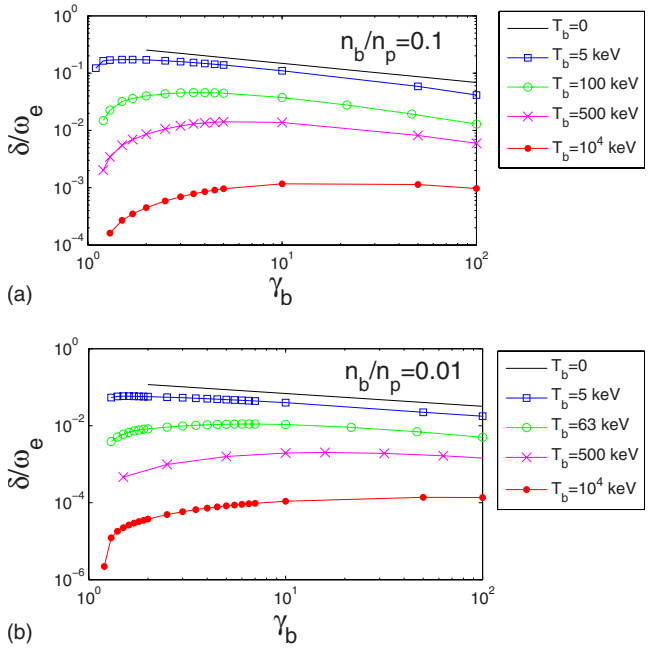

FIG. 14. (Color online) Maximum oblique growth rate $\delta_{\max}$ vs γ_b for varying T_b and (a) $n_b/n_p=0.1$ and (b) 0.01. $T_p=5$ keV in all cases. In the hydrodynamic, high-γ_b limit defined implicitly by Eq. (16), the growth rate scales such as $\gamma_b^{-1/3}$. The portion of each curve pertaining to the two-stream regime is excluded.

(18), all curves with $T_b \leq 50$ keV exhibit a kinetic scaling behavior $\delta_{\max} \propto T_b^{-1}$ in the high-T_b limit. However, they present a γ_b variation somewhat larger than predicted. This discrepancy may be attributed to the assumptions made in deriving Eqs. (18). In the opposite low-T_b limit, the curves significantly deviate from the kinetic law, though without exhibiting the T_b-independent behavior of Eq. (15), which defines the hydrodynamical regime.

For $n_b=0.1$ and $\gamma_b=2$, 5, and 10, the threshold temperature predicted from Eq. (16) is $T_b \sim 21$, 40, and 59 keV, respectively. For $n_b=0.01$, we have $T_b \sim 5$, 9, and 13 keV. All of these values compare reasonably well with the results of Figs. 13(a) and 13(b) even though the value obtained at $n_b=0.1$ and $\gamma_b=10$ exceeds the low-temperature domain of validity of the velocity spread (2). It is worth mentioning that the transition from the hydrodynamic to the kinetic regime encompasses a broad range in T_b, as previously found in Ref. [26].

A clearer view of the γ_b influence is provided in Fig. 14, where the evolution of $\delta_{\max}$ is plotted as a function of γ_b for various values of T_b and n_b/n_p. All finite-temperature curves with $T_b \leq 500$ keV approximately show the characteristic hydrodynamic $\gamma_b^{-1/3}$ scaling law at large γ_b. An estimate of the γ_b threshold above which this behavior holds directly follows from inverting Eq. (16). For $T_b=5$ keV and $n_b/n_p=(0.01, 0.1)$, this formula suggests a $\gamma_b^{-1/3}$ scaling law as soon as the beam turns weakly relativistic. For $n_b/n_p=0.1$, it predicts threshold values $\gamma_b \sim 2$ and ~7 for $T_b=20$ keV and 50 keV, respectively. For $n_b/n_p=0.01$ and $T_b=(20, 50)$ keV, the predicted values do not satisfy the assumption $\gamma_b T_b/m_e c^2 \ll 1$. Moreover, in contrast to the assumptions underlying Eq. (16), the high-γ_b behavior exhibited by the

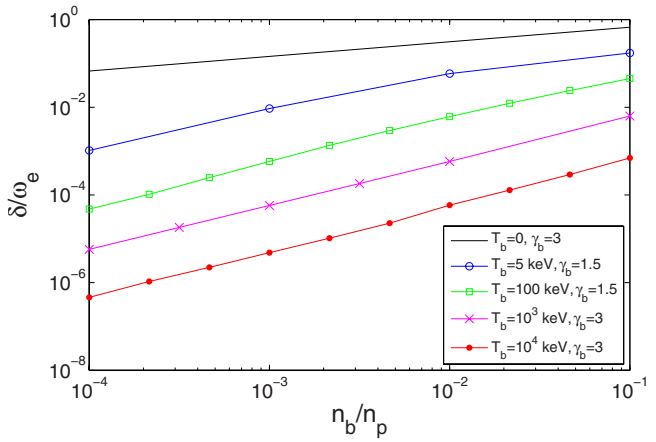

FIG. 15. (Color online) Maximum oblique growth rate $\delta_{\max}$ vs n_b/n_p for varying T_b and γ_b. Except for the cold case, $T_p=5$ keV. The three lower curves exhibit the kinetic n_b/n_p scaling law, whereas the one corresponding to $T_b=5$ keV shows a transition from the kinetic to the hydrodynamical $(n_b/n_p)^{1/3}$ scaling law.

finite-temperature systems of Fig. 14 does not point to an exact hydrodynamic regime because of a remaining dependence on the beam temperature ($\delta_{\max} \propto 1/\sqrt{T_b}$), for which we have not managed to derive an analytical expression.

Finally, let us address the density dependence of the maximum oblique growth rate. Figure 15 plots $\delta_{\max}$ vs n_b/n_p for various couples (γ_b, T_b). The curve corresponding to the cold case with $\gamma_b=3$ exhibits the expected $(n_b/n_p)^{1/3}$ scaling law, whereas the curves obtained for $(\gamma_b, T_b)=(1.5, 100$ keV) and (3,1000 keV) display a T_b^{-1} dependence typical of the kinetic regime in the whole range $10^{-4} < n_b/n_p < 10^{-1}$. In contrast, the curve corresponding to $(\gamma_b, T_b)=(1.5, 5$ keV) shows a transition between the cold and kinetic regimes around $n_b/n_p \sim 0.01$. This is in fair agreement with Eq. (16), which predicts a transition into the kinetic regime for a density ratio

$$\frac{n_b}{n_p} \leqslant \frac{32}{3^{3/2}} \left(\frac{T_b}{m_e c^2} \right)^{3/2} \frac{(1+\gamma_b^{-1})^3}{\gamma_b^{3/2}(1+\gamma_b^{-2})}. \tag{19}$$

For the latter set of values, the above threshold density ratio is $n_b/n_p \sim 0.01$, whereas it is >0.1 for the former cases. As already mentioned, Eq. (18), though yielding the correct scaling behaviors in T_b and n_b/n_p, overestimates by a factor of ~ 5 the kinetic regime growth rates of Figs. 13 and 15. Further analytical work is needed to derive more accurate analytical formulas, e.g., following the lines of Refs. [82,85]. which were restricted to the two-stream instability.

B. Most unstable wave vector

The wave vector of the fastest growing mode determines the shape and the size of the patterns generated through the linear phase. Its knowledge is critical for assessing the strength of the wave-particle coupling since it enters the expression of both the wave phase velocity and, given the amplitude of the dominant mode, the bounce frequency of the trapped particles [3,86]. Equating the latter with the linear growth rate yields a rough estimate of the saturated field energy within the single wave model [40,87,88].

Denoting $\mathbf{k}_{\max}=(k_{x,\max}, k_{z,\max})$ the wave vector of the dominant oblique mode for a given set of parameters $(n_b/n_p, \gamma_b, T_b, T_p)$, one could naively think that the dominant filamentation and two-stream modes are located at $\mathbf{k} \sim (k_{x,\max}, 0)$ and $\mathbf{k} \sim (0, k_{z,\max})$, respectively. While this assertion proves to be fairly correct regarding the two-stream mode, it does not hold for the filamentation mode when the oblique instability enters the kinetic regime.

The correlation of the two-stream and oblique modes is illustrated in Fig. 16 which compares the normalized k_z component of the fastest growing two-stream and oblique modes as a function of T_b for $n_b/n_p=0.1$, $T_p=5$ keV, and varying γ_b. The parallel wave vectors of the two instability classes are found to differ by less than 5% for each set of param-

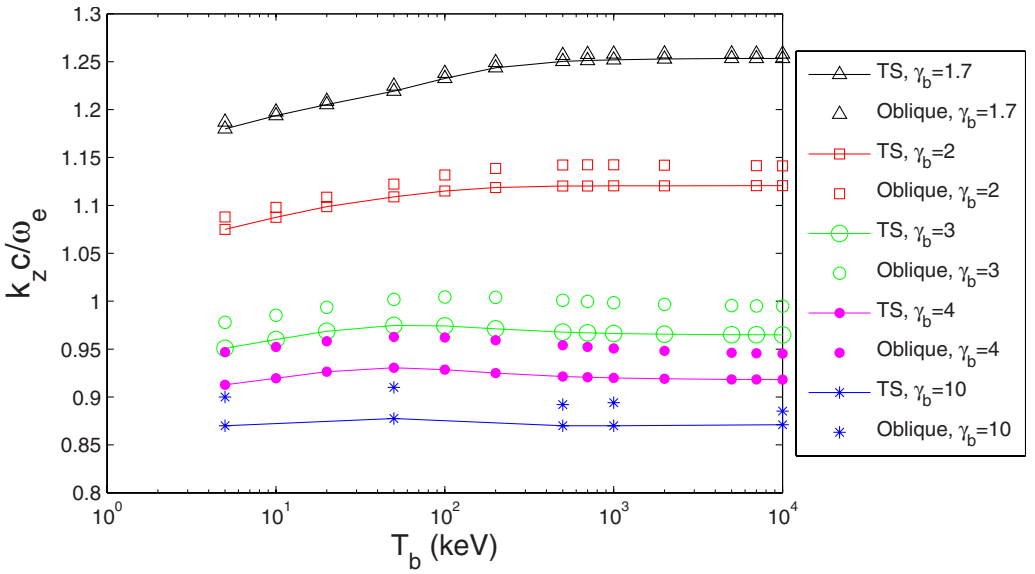

FIG. 16. (Color online) k_z component of the fastest growing two-stream and oblique modes as a function of the beam temperature T_b for $n_b/n_p=0.1$, $T_p=5$ keV and γ_b varying from 1.7 to 10. Two-stream modes govern the system for $\gamma_b=1.7$.

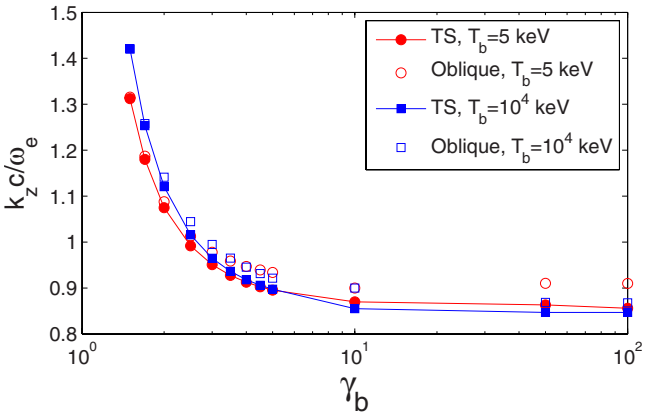

FIG. 17. (Color online) k_z component of the fastest growing two-stream and oblique modes as a function of the beam relativistic factor γ_b for $n_b/n_p=0.1$, $T_p=5$ keV and varying beam temperatures. Two-stream modes govern the system for γ_b close to 1.

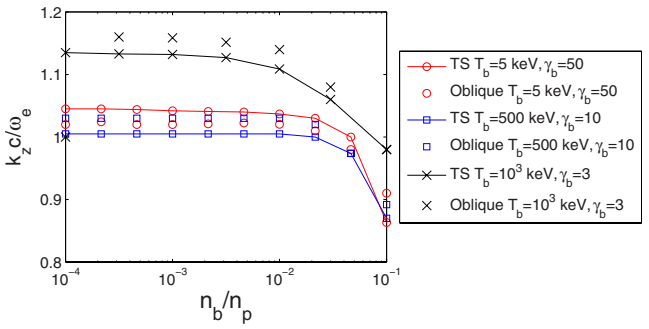

FIG. 18. (Color online) k_z component of the fastest growing two-stream and oblique modes as a function of the density ratio n_b/n_p for $T_p=5$ keV and varying beam temperatures and relativistic factors.

eters. Let us also note the weak variations of k_z over the broad range of T_b investigated. The slight changes in the slope of the curves seem correlated with the transition into the kinetic regime (Fig. 13). The coupling between two-stream and oblique modes is further depicted in Figs. 17 and 18 plotting the dependence of their k_z component upon γ_b and n_b/n_p. Again, k_z of both modes shows weak sensitivity to the system parameters, remaining close to the value $k_z \sim 1/\beta_b$ expected in the diluted-beam regime [26]

Figure 19 now compares the T_b dependence of the normalized k_x component of the fastest growing oblique and filamentation modes for the same range of parameters as above. Both modes exhibit a similar decrease at low T_b, but behave differently beyond $T_b \sim 50-100$ keV, that is, when the oblique instability enters the kinetic regime (Fig. 13) while the oblique wave vector then seems to saturate at a value $k_x \sim 0.5$ independent of γ_b, its filamentation counterpart steadily decreases with a $\sim T_b^{-1/2}$ scaling behavior. This dependence can be derived assuming that the dominant filamentation wave vector behaves similarly to the upper bound of the unstable domain $k_{\rm lim}$, which can be exactly expressed as [68],

$$k_{\rm lim}^2 = \frac{1}{2}[\mathcal{F}_2 - \mathcal{F}_0 + \sqrt{(\mathcal{F}_0 - \mathcal{F}_2)^2 + 4(\mathcal{F}_0\mathcal{F}_2 - \mathcal{F}_1^2)}], \quad (20)$$

where we have defined

$$\mathcal{F}_m = \sum_{\alpha=b,p} n_\alpha \mu_\alpha \beta_\alpha^m, \quad m \in \{0,1,2\}. \quad (21)$$

It can easily be verified that $k_{\rm lim} > 0$ for any set of nonzero β_α's, meaning that, whatever its temperatures, the beam-plasma system described by Maxwell-Jüttner distribution

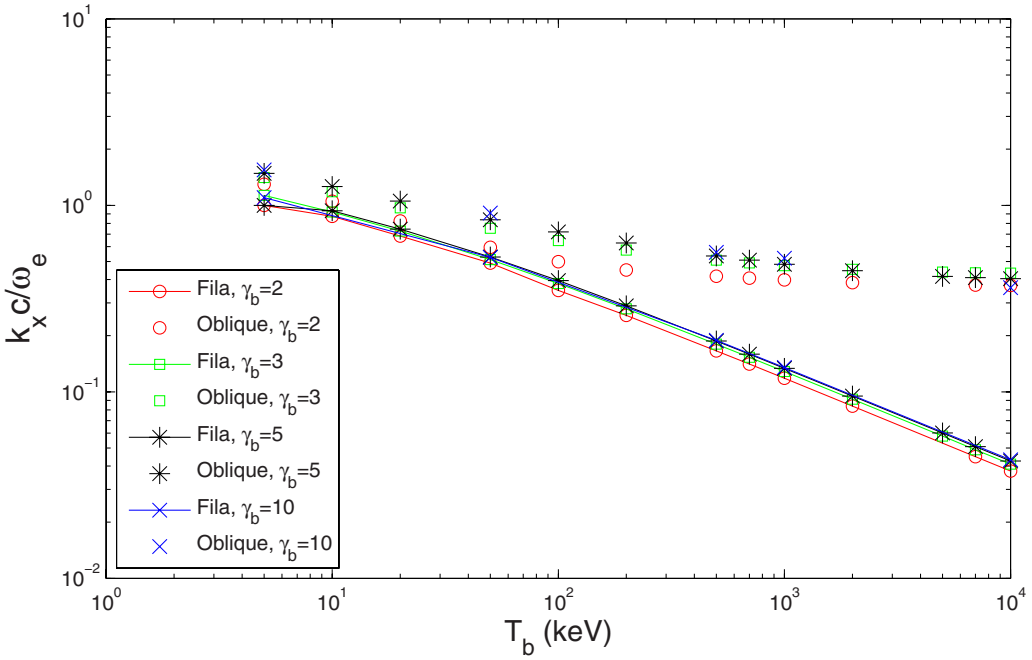

FIG. 19. (Color online) k_x component of the fastest growing filamentation and oblique modes as a function of the beam temperature T_b for $n_b/n_p=0.1$, $T_p=5$ keV and γ_b varying from 1.7 to 10. The two instabilities decouple beyond a threshold temperature.

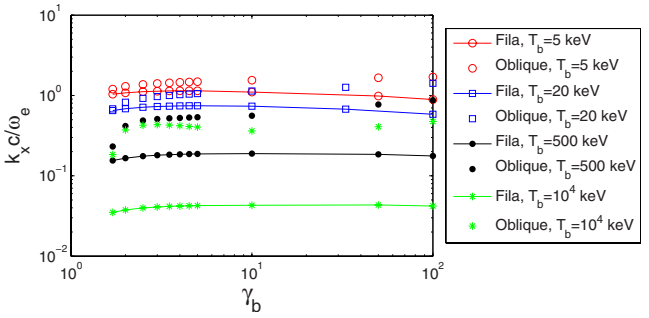

FIG. 20. (Color online) k_x component of the fastest growing filamentation and oblique modes as a function of the beam relativistic factor γ_b for $n_b/n_p=0.1$, $T_p=5$ keV and varying beam temperatures.

functions [1] still remains anisotropic enough to drive the filamentation instability. This feature differs markedly from the complete suppression of the instability known to arise in case of relativistic waterbag [40,63] or nonrelativistic Maxwellian [89,90] distribution functions. For the diluted-beam cold-plasma case (i.e., $n_b/n_p \ll 1$ and $T_p/m_e c^2 \ll 1$) considered here, it is straightforward to show that

$$k_{\mathrm{lim}} \sim \beta_b \sqrt{\left(\frac{n_b}{n_p}\right)\left(\frac{m_e c^2}{T_b}\right)}, \tag{22}$$

in the limit $(n_b/n_p)(T_b/T_p) \gg 1$. Note that a similar scaling law can been derived with waterbag distributions assuming a proper definition of the beam temperature [50,52].

The above formula predicts a weak dependence of the dominant filamentation wave vector upon γ_b in the relativistic regime. This behavior is confirmed in Fig. 20 which plots the evolution of k_x as a function of γ_b for various values of T_b. The corresponding variations of the k_x component of the dominant oblique mode are more pronounced, most notably in the low-γ_b limit. In the high-γ_b limit, k_x steadily rises as expected in the hydrodynamical regime. Moreover, Fig. 21 confirms the predicted $\sqrt{n_b/n_p}$ scaling law of the dominant filamentation wave vector for various sets of (γ_b, T_b).

To conclude this study of the dominant unstable oblique modes, let us further emphasize their mostly electrostatic character, a property already exploited to derive the formulas of Sec. IV A. Indeed, as shown in Figs. 22(a) and 22(d) for varying sets of parameters, the electric-field component of the fastest growing oblique modes prove to be, in a good approximation, parallel to their wave vector. We have made use of the relation $E_x(\omega,\mathbf{k})/E_z(\omega,\mathbf{k}) = (k_x^2 - \omega^2\epsilon_z z)/(k_x k_z + \omega^2 \epsilon_{xz})$ [50]. The quasielectrostatic nature of the oblique modes has long been known to hold in the diluted-beam case [23,24,26], as exemplified in Fig. 22(a) where the angle between $\mathbf{k}_{\max}$ and $\mathbf{E}$ is measured to be $\varphi_{\mathbf{k}}=0.08$. We find here that it may also apply in high beam density configurations governed by oblique modes such as those considered in Figs. 22(b) and 22(c), yielding $\varphi_{\mathbf{k}}=0.23$ and $\varphi_{\mathbf{k}}=0.1$, respectively. Note the large electrostatic x component of the electric field associated with *filamentation* modes in these cases, which results from different relativistic inertias and temperatures between the beam and plasma populations [41,79]. Finally, Fig. 22(d) shows that the electrostatic approximation remains accurate enough ($\varphi_{\mathbf{k}}=0.43$, i.e., $\cos\varphi_{\mathbf{k}}=0.91$) for a filamentation-governed system characterized by two separated growth rate maxima. The observed broad range of validity of the electrostatic approximation could facilitate further analytical work on the oblique instability given the more tractable form of the related dispersion relation [26].

V. CONCLUSIONS

We have carried out a comprehensive analysis of the 2D unstable spectrum of a relativistic unmagnetized beam-plasma system described by 3D drifting Maxwell-Jüttner distribution functions within a fully electromagnetic kinetic formalism. The present work complements the results of Ref. [58], which mostly dealt with the hierarchy of the three identified instability classes in the system-parameter space. Here,

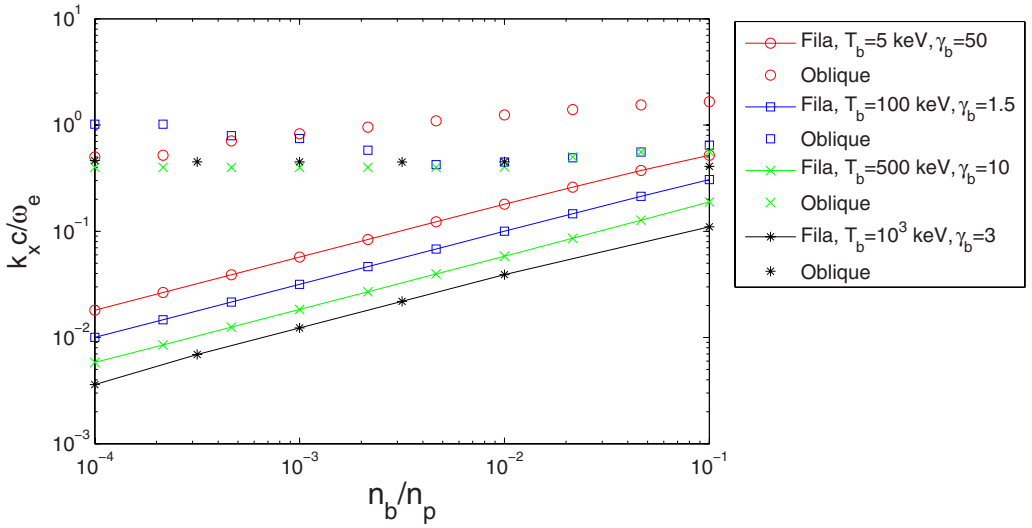

FIG. 21. (Color online) k_x component of the fastest growing filamentation modes as a function of the density ratio n_b/n_p for $T_p=5$ keV and varying T_b and γ_b.

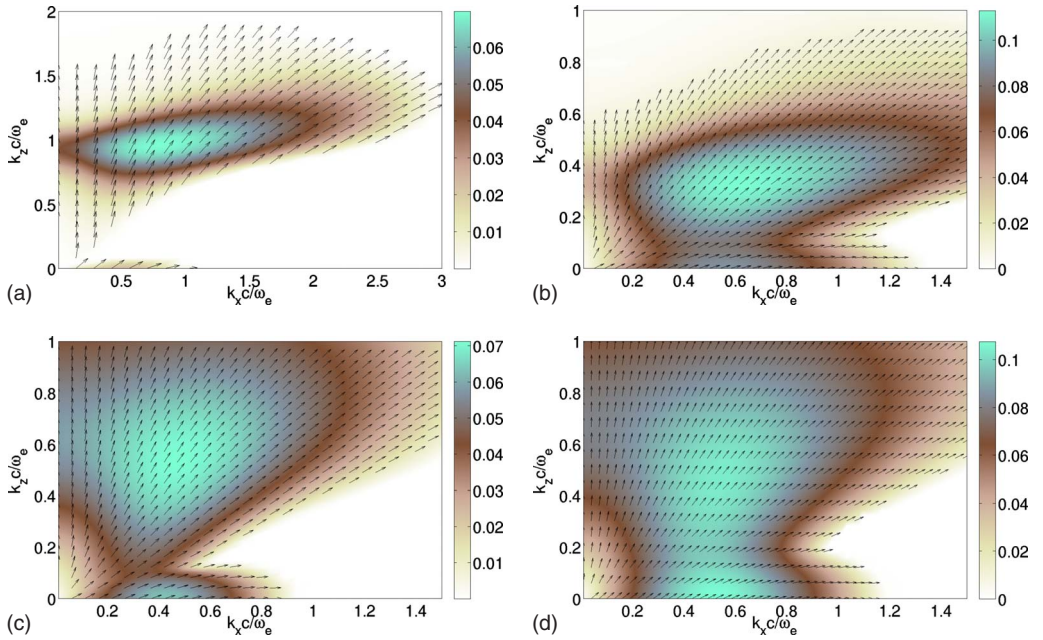

FIG. 22. (Color online) Overlay of the electric field orientation in (x,z) configuration space and of the growth rate in $\mathbf{k}$ space for varying system parameters: (a) $n_b/n_p=0.1$, $\gamma_b=4$, $T_b=500$ keV, $T_p=5$ keV; (b) $n_b/n_p=0.7$, $\gamma_b=3$, $T_b=500$ keV, $T_p=5$ keV (c) $n_b/n_p=1$, $\gamma_b=1.2$, $T_b=500$ keV, $T_p=5$ keV; and (d) $n_b/n_p=1$, $\gamma_b=1.2$, $T_b=300$ keV, $T_p=5$ keV.

the changes in the characteristics of the dominant modes when crossing a transition boundary are investigated in more detail. In particular, we have highlighted the discontinuous variation of the dominant wave vector during the filamentation-to-oblique transition. Most of this work, however, has been devoted to a parametric study of the domain governed by oblique modes, aiming at inferring the main scaling laws of the dominant modes' properties with respect to the beam parameters, as well as gauging the validity of existing formulas obtained within simplifying assumptions [3]. Most notably, we have found that the variations in the maximum oblique growth rate with the beam density, temperature, and relativistic factor essentially exhibit the scaling laws previously derived for simpler model distribution functions in the hydrodynamical and kinetic limits. Provisos must be added, though: the transition between these two regimes generally covers a broad parameter range, and their identification may only be partial. This is the case for the so-called hydrodynamical regime, wherein the typical $\gamma_b^{-1/3}$ and $(n_b/n_p)^{1/3}$ behaviors are recovered, yet with a residual thermal dependence for which an analytical expression has yet to be derived (see Figs. 14 and 15). In the kinetic regime, whereas the computed growth rates confirm the expected n_b/n_p and T_b^{-1} scaling laws, they turn out to be significantly lower than the theoretical estimate (18). Moreover, we have demonstrated the correlated variations of the fastest growing oblique and two-stream modes. This coupling, pointed out a long time ago in simpler cases [3], stems from the essential electrostatic character of the oblique modes, which is here shown to hold in a parameter range extending well beyond the diluted beam limit addressed in the early studies. Regarding the coupling with the filamentation instability, the perpendicular k_x component of the dominant oblique mode follows that of the dominant filamentation mode throughout the hydrodynamic regime. Once in the kinetic regime, it saturates to a finite value, while the filamentation unstable domain collapses toward $k_x=0$ [see Figs. 19 and 21 and Eq. (22)].

To conclude, we stress that the present work has not accounted for the effects of varying plasma temperatures and mobile ions. The electron-ion and ion-ion instabilities arising when allowing for relativistic ions are of particular importance in a number of astrophysical scenarios because they are widely believed to drive collisionless shocks [10,91,92]. They will be addressed within the present unified formalism in a forthcoming study.

ACKNOWLEDGMENTS

We acknowledge enriching discussions with Gustavo Wouchuk. This work has been partially achieved under Project No. ENE2009-09276 of the Spanish Ministerio de Educación y Ciencia, and PAI08-0182-3162 of the Consejería de Educación y Ciencia de la Junta de Comunidades de Castilla-La Mancha.

APPENDIX: SIMPLIFIED EXPRESSIONS OF THE DIELECTRIC TENSOR ELEMENTS

After some lengthy calculations, the tensor elements involved in the dispersion Eq. (4) may be written in the form

$$\epsilon_{xx} = 1 - \sum_{j=b,p} \frac{n_j}{\omega^2}(\omega - k_z\beta_j)\mu_j\Lambda_j[\mathcal{A}_j \cos^2\theta + \mathcal{B}_j \sin^2\theta + 2\mathcal{C}_j \sin\theta\cos\theta],$$

$$\epsilon_{zz} = 1 + \sum_{j=b,p} \frac{n_j}{\omega^2}\mu_j\beta_j^2 - \frac{n_j}{\omega^2}(\omega - k_z\beta_j)\mu_j\Lambda_j[\mathcal{A}_j \sin^2\theta + \mathcal{B}_j \cos^2\theta - 2\mathcal{C}_j \sin\theta\cos\theta],$$

$$\epsilon_{xz} = -\sum_{j=b,p} \frac{n_j}{\omega^2}(\omega - k_z\beta_j)\mu_j\Lambda_j[(\mathcal{B}_j - \mathcal{A}_j)\sin\theta\cos\theta + \mathcal{C}_j(\cos^2\theta - \sin^2\theta)], \tag{A1}$$

where θ is the angle between $\mathbf{k}$ and the beam z axis, $\Lambda_j = \mu_j[4\pi\gamma_j^2 K_2(\mu_j/\gamma_j)]^{-1}$ and

$$\mathcal{A}_j = 2\pi\int_{-1}^{1} du\,\gamma \frac{\rho_j^2 + 2\nu_j^2 + (\rho_j^2 - \nu_j^2)^{1/2}(\rho_j^2 + 2\nu_j^2) + \nu_j^2(\rho_j^2 - \nu_j^2)}{(\omega - ku)(\rho_j^2 - \nu_j^2)^{5/2}} \exp[-(\rho_j^2 - \nu_j^2)^{1/2}],$$

$$\mathcal{B}_j = 2\pi\int_{-1}^{1} du\,\gamma^3 u^2 \frac{2\rho_j^2 + \nu_j^2 + (\rho_j^2 - \nu_j^2)^{1/2}(2\rho_j^2 + \nu_j^2) + \rho_j^2(\rho_j^2 - \nu_j^2)}{(\omega - ku)(\rho_j^2 - \nu_j^2)^{5/2}} \exp[-(\rho_j^2 - \nu_j^2)^{1/2}],$$

$$\mathcal{C}_j = -2\pi\nu_j\int_{-1}^{1} du\,\rho_j\gamma^2 u \frac{3 + 3(\rho_j^2 - \nu_j^2)^{1/2} + \rho_j^2 - \nu_j^2}{(\omega - ku)(\rho_j^2 - \nu_j^2)^{5/2}} \exp[-(\rho_j^2 - \nu_j^2)^{1/2}]. \tag{A2}$$

We have defined $\rho_j = \mu_j(1 - \beta_j u\cos\theta)\gamma$, $\nu_j = \mu_j\beta_j \sin\theta$, and $\gamma = (1-u^2)^{-1/2}$.

[1] R. C. Davidson, in *Handbook of Plasma Physics*, edited by M. N. Rosenbluth and R. Z. Galeev (North-Holland, Amsterdam, 1983), Vol. 1.

[2] R. B. Miller, *An Introduction to the Physics of Intense Charged Particle Beams* (Plenum, New York, 1982).

[3] R. N. Sudan, in *Handbook of Plasma Physics*, edited by M. N. Rosenbluth and R. Z. Galeev (North-Holland, Amsterdam, 1984), Vol. 2.

[4] M. Tabak, J. Hammer, M. E. Glinsky, W. L. Kruer, S. C. Wilks, J. Woodworth, E. M. Campbell, M. D. Perry, and R. J. Mason, Phys. Plasmas **1**, 1626 (1994).

[5] M. Tabak *et al.*, Phys. Plasmas **12**, 057305 (2005).

[6] Y. Sentoku, K. Mima, S. Kojima, and H. Ruhl, Phys. Plasmas **7**, 689 (2000).

[7] V. M. Malkin and N. J. Fisch, Phys. Rev. Lett. **89**, 125004 (2002).

[8] J. T. Mendonça, P. Norreys, R. Bingham, and J. R. Davies, Phys. Rev. Lett. **94**, 245002 (2005).

[9] J. Honrubia and J. Meyer-ter-Vehn, Nucl. Fusion **46**, L25 (2006).

[10] M. Medvedev and A. Loeb, Astrophys. J. **526**, 697 (1999).

[11] M. Gedalin, E. Gruman, and D. B. Melrose, Phys. Rev. Lett. **88**, 121101 (2002).

[12] R. A. Fonseca, L. O. Silva, J. W. Tonge, W. B. Mori, and J. M. Dawson, Phys. Plasmas **10**, 1979 (2003).

[13] T. Piran, Rev. Mod. Phys. **76**, 1143 (2005).

[14] C. Jaroschek, H. Lesch, and R. Treumann, Astrophys. J. **618**, 822 (2005).

[15] R. C. Tautz and I. Lerche, Astrophys. J. **653**, 447 (2006).

[16] K. I. Nishikawa, P. E. Hardee, C. B. Hededal, and G. J. Fishman, Astrophys. J. **642**, 1267 (2006).

[17] T. Kato, Astrophys. J. **668**, 974 (2007).

[18] R. Schlickeiser and I. Lerche, Astron. Astrophys. **476**, 1 (2007).

[19] D. Bohm and E. P. Gross, Phys. Rev. **75**, 1851 (1949).

[20] E. S. Weibel, Phys. Rev. Lett. **2**, 83 (1959).

[21] B. Fried, Phys. Fluids **2**, 337 (1959).

[22] S. A. Bludman, K. M. Watson, and M. N. Rosenbluth, Phys. Fluids **3**, 747 (1960).

[23] Y. B. Faĭnberg, V. D. Shapiro, and V. Shevchenko, Sov. Phys. JETP **30**, 528 (1970).

[24] L. I. Rudakov, Sov. Phys. JETP **32**, 1134 (1971).

[25] G. Kalman, C. Montes, and D. Quemada, Phys. Fluids **11**, 1797 (1968).

[26] R. L. Ferch and R. N. Sudan, Plasma Phys. **17**, 905 (1975).

[27] H. Lee and L. E. Thode, Phys. Fluids **26**, 2707 (1983).

[28] T. Tajima, Phys. Fluids **22**, 1157 (1979).

[29] M. E. Jones, Phys. Fluids **26**, 1928 (1983).

[30] H. S. Uhm, Phys. Fluids **26**, 3098 (1983).

[31] H. S. Uhm, J. Appl. Phys. **56**, 2041 (1984).

[32] R. C. Davidson, in *Handbook of Plasma Physics*, edited by M. N. Rosenbluth and R. Z. Galeev (North-Holland, Amsterdam, 1984), Vol. 2.

[33] F. Califano, F. Pegoraro, S. V. Bulanov, and A. Mangeney, Phys. Rev. E **57**, 7048 (1998).

[34] C. Jaroschek, H. Lesch, and R. Treumann, Astrophys. J. **616**, 1065 (2004).

[35] L. Gremillet, D. Bénisti, E. Lefebvre, and A. Bret, Phys. Plasmas **14**, 040704 (2007).

[36] X. Kong, J. Park, C. Ren, Z. M. Sheng, and J. Tonge, Phys. Plasmas **16**, 032107 (2009).

[37] R. Lee and M. Lampe, Phys. Rev. Lett. **31**, 1390 (1973).

[38] J. R. Cary, L. E. Thode, D. S. Lemons, M. E. Jones, and M. A. Mostrom, Phys. Fluids **24**, 1818 (1981).

[39] M. Honda, Phys. Rev. E **69**, 016401 (2004).

[40] L. O. Silva, R. A. Fonseca, J. W. Tonge, W. B. Mori, and J. M. Dawson, Phys. Plasmas **9**, 2458 (2002).

[41] M. Tzoufras, C. Ren, F. S. Tsung, J. W. Tonge, W. B. Mori, M. Fiore, R. A. Fonseca, and L. O. Silva, Phys. Rev. Lett. **96**, 105002 (2006).

[42] U. Schaefer-Rolffs, I. Lerche, and R. Schlickeiser, Phys. Plasmas **13**, 012107 (2006).
[43] R. C. Tautz and I. Lerche, J. Phys. A **40**, F677 (2007).
[44] M. Tzoufras, C. Ren, F. S. Tsung, J. W. Tonge, W. B. Mori, M. Fiore, R. A. Fonseca, and L. O. Silva, Phys. Plasmas **14**, 062108 (2007).
[45] L. A. Cottrill, A. B. Langdon, B. F. Lasinski, S. M. Lund, K. Molvig, M. Tabak, R. P. J. Town, and E. A. Williams, Phys. Plasmas **15**, 082108 (2008).
[46] O. Polomarov, I. Kaganovich, and G. Shvets, Phys. Rev. Lett. **101**, 175001 (2008).
[47] A. Karmakar, N. Kumar, A. Pukhov, O. Polomarov, and G. Shvets, Phys. Plasmas **15**, 120702 (2008).
[48] B. B. Godfrey, W. R. Shanahan, and L. E. Thode, Phys. Fluids **18**, 346 (1975).
[49] F. Califano, R. Prandi, F. Pegoraro, and S. V. Bulanov, Phys. Rev. E **58**, 7837 (1998).
[50] A. Bret, M.-C. Firpo, and C. Deutsch, Phys. Rev. E **70**, 046401 (2004).
[51] A. Bret, M.-C. Firpo, and C. Deutsch, Phys. Rev. E **72**, 016403 (2005).
[52] A. Bret, M.-C. Firpo, and C. Deutsch, Phys. Rev. Lett. **94**, 115002 (2005).
[53] L. O. Silva, R. A. Fonseca, J. W. Tonge, and W. B. Mori, Bull. Am. Phys. Soc. **46**, 205 (2001).
[54] A. Bret and C. Deutsch, Phys. Plasmas **13**, 042106 (2006).
[55] J. C. Adam, A. Héron, and G. Laval, Phys. Rev. Lett. **97**, 205006 (2006).
[56] C. Ren, M. Tzoufras, J. Tonge, W. B. Mori, F. S. Tsung, M. Fiore, R. A. Fonseca, L. O. Silva, J. C. Adam, and A. Héron, Phys. Plasmas **13**, 056308 (2006).
[57] T. Okada and K. Ogawa, Phys. Plasmas **14**, 072702 (2007).
[58] A. Bret, L. Gremillet, D. Bénisti, and E. Lefebvre, Phys. Rev. Lett. **100**, 205008 (2008).
[59] F. Jüttner, Ann. Phys. **339**, 856 (1911).
[60] P. Wright and G. R. Hadley, Phys. Rev. A **12**, 686 (1975).
[61] D. Cubero, J. Casado-Pascual, J. Dunkel, P. Talkner, and P. Hänggi, Phys. Rev. Lett. **99**, 170601 (2007).
[62] G. Amelino-Camelia, Nature (London) **450**, 801 (2007).
[63] P. H. Yoon and R. C. Davidson, Phys. Rev. A **35**, 2718 (1987).
[64] R. C. Davidson and P. Yoon, Phys. Fluids B **1**, 195 (1989).
[65] P. Yoon, Phys. Plasmas **14**, 024504 (2007).
[66] U. Schaefer-Rolffs, I. Lerche, and R. Schlickeiser, Phys. Plasmas **15**, 062105 (2008).
[67] S. Ichimaru, *Basic Principles of Plasma Physics* (W. A. Benjamin, Inc., Reading, Massachusetts, 1973).
[68] L. Gremillet (to be published).
[69] S. Bellavia, M. Macconi, and B. Morini, Comput. Optim. Appl. **28**, 31 (2004).
[70] S. Bellavia, M. Macconi, and B. Morini, Appl. Numer. Math. **44**, 257 (2003).
[71] A. Bret and C. Deutsch, Phys. Plasmas **12**, 082704 (2005).
[72] A. Bret and C. Deutsch, Phys. Plasmas **14**, 119902 (2007).
[73] J. Wiersma and A. Achterberg, Astron. Astrophys. **428**, 365 (2004).
[74] F. Califano, D. Del Sarto, and F. Pegoraro, Phys. Rev. Lett. **96**, 105008 (2006).
[75] J. M. Hill, M. H. Key, S. P. Hatchett, and R. R. Freeman, Phys. Plasmas **12**, 082304 (2005).
[76] C. Deutsch, A. Bret, M.-C. Firpo, and P. Fromy, Phys. Rev. E **72**, 026402 (2005).
[77] Y. Sentoku, K. Mima, P. Kaw, and K. Nishikawa, Phys. Rev. Lett. **90**, 155001 (2003).
[78] S. Atzeni, A. Schiavi, J. J. Honrubia, X. Ribeyre, G. Schurtz, P. Nicola, M. Olazabal-LoumŽ, C. Bellei, R. G. Evans, and J. R. Davies, Phys. Plasmas **15**, 056311 (2008).
[79] A. Bret, L. Gremillet, and J. C. Bellido, Phys. Plasmas **14**, 032103 (2007).
[80] M. E. Dieckmann, J. T. Frederiksen, A. Bret, and P. K. Shukla, Phys. Plasmas **13**, 112110 (2006).
[81] R. Buschauer and G. Benford, Mon. Not. R. Astron. Soc. **179**, 99 (1977).
[82] A. Magneville, J. Plasma Phys. **44**, 191 (1990).
[83] J. Weatherall, Astrophys. J. **428**, 261 (1994).
[84] A. B. Mikhailovskii, *Theory of Plasma Instabilities* (Consultant Bureau, New York, 1974), Vol. 2.
[85] A. Magneville, J. Plasma Phys. **44**, 213 (1990).
[86] R. Davidson, C. Wagner, D. Hammer, and I. Haber, Phys. Fluids **15**, 317 (1972).
[87] W. M. Manheimer, Phys. Fluids **14**, 579 (1971).
[88] T.-Y. B. Yang, J. Arons, and A. B. Langdon, Phys. Plasmas **1**, 3059 (1994).
[89] A. Bret and C. Deutsch, Phys. Plasmas **13**, 022110 (2006).
[90] M. Lazar, R. Schlickeiser, and P. K. Shukla, Phys. Plasmas **13**, 102107 (2006).
[91] J. T. Frederiksen, C. B. Hebedal, T. Haugbolle, and A. Nordlund, Astrophys. J. **608**, L13 (2004).
[92] A. Spitkovsky, Astrophys. J. **673**, L39 (2008).